aerospace

MDPI

Article

Energy-Saving Low- and Medium Cavitation Temperature Deicer Theory and Experimental Testing

Victor F. Petrenko

Thayer School of Engineering, Dartmouth College, Hanover, NH 03755, USA; victor.f.petrenko@dartmouth.edu

Abstract

This manuscript presents the theory and experimental validation of low- and medium-temperature deicing technology that advances the recently developed Ice Cavitation Deicing (ICD) method. Conventional high-temperature ICD (HTICD) efficiently removes ice by explosively vaporizing a thin interfacial melted layer but operates at heating rates above 10^6 K/s, high voltage, and maximum temperatures exceeding 400 °C. This study develops Low-Temperature and Medium-Temperature Ice Cavitation Deicing (LTICD and MTICD), extending ICD into the previously unexplored intermediate heating-rate regime. Analytical modeling based on energy conservation, transient heat diffusion, water thermodynamics, and thermal-stress analysis was combined with finite-element simulations and experimental testing. Several foil materials were evaluated over heating rates of approximately 10^4–10^7 K/s using capacitor banks of 0.1–35 mF. Experiments demonstrated effective removal of thick and thin ice at cavitation temperatures of approximately 120–200 °C, substantially below those of HTICD. The lower operating temperatures and heating rates reduce thermal stress, voltage, and current, enable practical low-voltage electrolytic capacitors, and expand the range of suitable materials. Thus, LTICD and MTICD provide a lower-temperature, more practical electrical architecture for future aircraft ice-protection systems.

Keywords: aircraft de-icing; electro-thermal de-icing; cavitation; explosive vaporization; ice protection systems; energy efficiency

1. Introduction

The accumulation of ice on aerodynamic surfaces remains a major safety and operational challenge for modern aviation [1]. Ice accretion degrades aerodynamic performance, increases drag and weight, and may lead to loss of lift or controllability. Conventional electrothermal deicing systems are reliable but often require more electrical power or bleed air than is readily available on small, medium-sized, and unmanned aircraft. In contrast, electro-impulse deicers (EID) consume relatively little energy but introduce structural fatigue, additional mechanical complexity, and long-term durability concerns.

Repetitive high-power electrothermal systems, including Pulse Electro-Thermal Deicing (PETD) [2,3] and cyclic deicers [4–6], substantially reduce energy consumption and average power requirements. However, after the ice/structure interface has melted, these systems still rely primarily on aerodynamic forces or gravity to remove the detached ice. Thus, there remains a need for a low-energy deicing method capable of actively ejecting ice while avoiding excessive structural loading and high continuous power consumption. Ice Cavitation Deicing (ICD) was recently introduced as an alternative approach that uses

Check for updates

Academic Editor: Sergey Leonov

Received: 10 August 2026
Revised: 11 September 2026
Accepted: 11 September 2026
Published: 14 September 2026

Copyright: © 2026 by the author. Licensee MDPI, Basel, Switzerland. This article is an open access article distributed under the terms and conditions of the Creative Commons Attribution (CC BY) license.

the melted interfacial water layer itself to generate the force required for ice removal [7]. In ICD, a thin water layer at the ice/heater interface is rapidly heated to the temperature of explosive vaporization. The resulting cavitation event produces a short, high-pressure pulse that ejects the ice layer from the surface. The first generation of ICD, hereafter referred to as High-Temperature Ice Cavitation Deicing (HTICD), operated on the high-temperature branch of homogeneous water nucleation at heating rates exceeding 10^6 K/s and cavitation temperatures near 300 °C [8,9]. HTICD demonstrated effective ice removal, with measured ice-ejection velocities of up to 10 m/s. However, its high operating temperature can produce foil temperatures exceeding 400 °C in ice-free regions, resulting in high thermal stresses, restricted material selection, and the need for high-voltage film-capacitor energy-storage systems.

The possibility of reducing these temperatures depends strongly on the relationship between the homogeneous nucleation temperature of water and its heating rate. Although this relationship has been investigated extensively, experimentally validated data are concentrated primarily in the low-heating-rate region (10^2–10^4 K/s) and the very high-heating-rate region (10^6–10^9 K/s). As summarized by Skripov et al. [10], reliable experimental data in the intermediate range of approximately 10^4–10^6 K/s remain scarce, with only limited measurements reported for rapidly heated SS304 wire [11]. This intermediate regime is particularly important for ICD because operation within it could potentially initiate explosive vaporization at substantially lower temperatures than those required for HTICD.

A further knowledge gap concerns the heater materials used to investigate explosive water vaporization. Previous studies have predominantly employed platinum or gold microheaters because of their stable electrical properties and suitability for resistance thermometry. Comparable investigations using practical engineering foil materials suitable for deicer construction, such as precipitation-hardened stainless steel, titanium alloys, and Invar, remain very limited. Consequently, it has not been established whether reliable cavitation-driven ice removal can be achieved with such materials at intermediate heating rates and reduced operating temperatures.

The objective of the present work was therefore to determine whether efficient ICD operation can be extended from the high-temperature regime to the low- and intermediate-temperature regimes. We hypothesized that cavitation deicing within the transition heating-rate range could substantially reduce the operating temperature, thermal stress, and electrical requirements of HTICD while preserving its impulse ice-ejection mechanism. Experiments were conducted over heating rates of approximately 10^4–10^7 K/s using capacitor banks ranging from 0.1 to 35 mF and several engineering foil materials, including SS17-7PH stainless steel, titanium Grade 1, titanium Grade 5, Invar, and SS304, with different thicknesses and aspect ratios. These combinations provided access to the low-, intermediate-, and high-heating-rate nucleation regimes.

The effects of heating rate, applied energy density, foil material, surface treatment, and support structure on deicing performance and ice-ejection velocity were investigated experimentally. Analytical calculations and finite-element simulations were used to interpret the measurements and to develop practical design guidelines. An analytical design methodology incorporating energy conservation, transient heat transfer, and thermal-stress analysis was developed and evaluated against the experimental results. The resulting Low-Temperature Ice Cavitation Deicing (LTICD) and Medium-Temperature Ice Cavitation Deicing (MTICD) regimes demonstrated effective removal of both thick and thin ice at substantially lower operating temperatures than HTICD.

2. Analytical Theory and Finite Element Analysis (FEA)

The operation of Ice Cavitation Deicing (ICD) is governed by two fundamental requirements. First, the interfacial water layer must reach the heating-rate-dependent nucleation temperature, $T_N(\dot{T})$. Second, the electrical energy delivered to the ICD must be sufficient to heat the foil and the adjacent substrate and ice/water layers until this condition is attained.

Skripov et al. [10] presented the experimentally established relationship between homogeneous nucleation temperature and heating rate. The available experimental data define two well-characterized regions: the low-temperature branch (heating rates below approximately 10^4 K/s) and the high-temperature branch (above approximately 10^6 K/s). Reliable experimental data remain scarce in the intermediate heating-rate range.

The present study focuses primarily on this intermediate region (approximately 10^4–10^6 K/s), where Sazhin et al. [12] proposed the following approximation for the nucleation temperature:

$$T_N = 385 + 160 \cdot \tanh\left(\frac{\dot{T}}{10^5}\right) \quad (1)$$

where T_N is the nucleation temperature in K and $\dot{T}$ is the heating rate (K/s). The resulting dependence is shown in Figure 1.

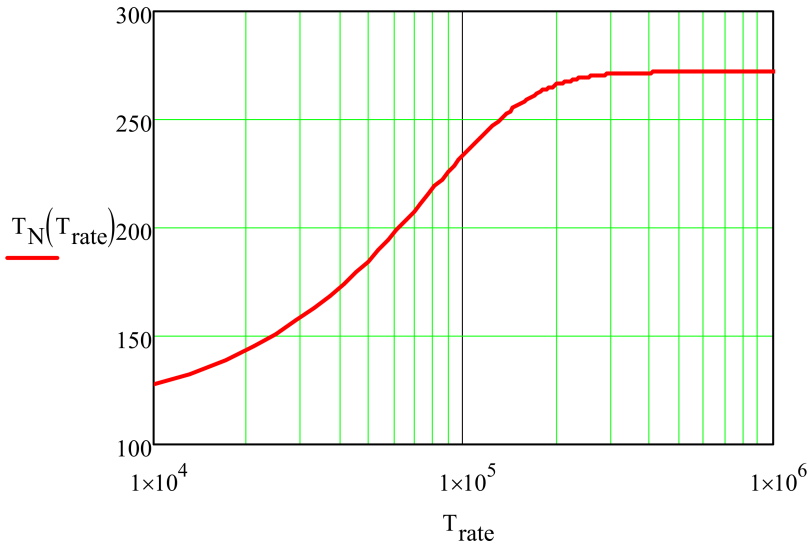


Figure 1. Nucleation temperature, T_N, °C vs. heating rate T_{rate} (°C/s).

The low-temperature branch provides the basis for Low-Temperature Ice Cavitation Deicing (LTICD), whereas the high-temperature branch was previously used for High-Temperature Ice Cavitation Deicing (HTICD) [7]. The present study also investigates the previously unexplored transition region centered near 10^5 K/s.

2.1. ICD Minimum Energy Requirement Calculations

The minimum energy density required for ICD was estimated using the First Law of Thermodynamics by accounting for the energy required to heat the metal foil, the adjacent substrate, and the ice layer to the nucleation temperature. At the threshold operating condition, the required energy density is:

$$Q_{rate} = (T_N - T_0)\cdot(\rho_S \cdot C_S \cdot \lambda_S + t_m \cdot \rho_m \cdot C_m) + (q_i + (T_N - 0\ ^\circ\mathrm{C}) \cdot C_w) \cdot \rho_i \cdot l_w + (T_m - T_0) \cdot C_i \rho_i \cdot \lambda_i \quad (2)$$

where Q_{rate} is the minimum ICD energy density, T_N is the nucleation temperature, T_0 is the initial temperature, q_i is the latent heat of melting, and the remaining symbols have their

usual thermophysical meanings. The subscripts m, S, and i denote the metal foil, substrate, and ice, respectively.

$$\lambda = \left(\frac{t_p \cdot k}{C \cdot \rho}\right)^{1/2} \tag{3}$$

where t_p is the pulse duration and k, C, and ρ are the thermal conductivity, specific heat, and density of the corresponding material. For the overdamped discharge circuit used throughout this study,

$$t_p \approx R_{tot} \cdot C_C \tag{4}$$

where R_{tot} is the total power-circuit resistance and C_C is the capacitance of the capacitor bank. Equation (4) provides a good approximation of the pulse duration. The thickness of the melted water layer was also estimated using the classical two-phase Stefan (Neumann) solution [13,14]:

$$l_w(T_{rate}, T_i) = 2 \cdot \lambda_{St}(T_{rate}, T_i) \cdot \sqrt{\alpha_{dw} \cdot \frac{T_N(T_{rate})}{T_{rate}}} \tag{5}$$

where λ_{St} is the Stefan (Neumann) similarity parameter, obtained as the numerical root of the corresponding transcendental equation:

$$\frac{k_w \cdot T_{ICD}(T_{rate}) \cdot e^{-\lambda_S{}^2}}{\sqrt{\pi \cdot \alpha_{dw}} \cdot \mathrm{erf}(\lambda_S)} + \frac{k_i \cdot T_i \cdot e^{-\lambda_S{}^2 \cdot \frac{\alpha_{dw}}{\alpha_{di}}}}{\sqrt{\pi \cdot \alpha_{di}} \cdot erfc\left(\sqrt{\lambda_S \cdot \frac{\alpha_{dw}}{\alpha_{di}}}\right)} = \rho_w \cdot q_i \cdot \lambda_{St} \cdot \sqrt{\alpha_{dw}} \tag{6}$$

where α_{dw} is water diffusivity and α_{di} is ice diffusivity.

Both approaches were compared with finite-element simulations. The COMSOL calculations consistently showed that the thermal diffusion length predicted the melted-layer thickness more accurately than the classical Stefan solution, which systematically overestimated the melt thickness under the rapid heating conditions encountered in ICD. Consequently, the diffusion-length approximation was adopted for the engineering design calculations presented below, while the Stefan solution was retained for comparison.

Figure 2 presents the predicted nucleation temperature and minimum ICD energy density as functions of heating rate using Equations (2)–(4).

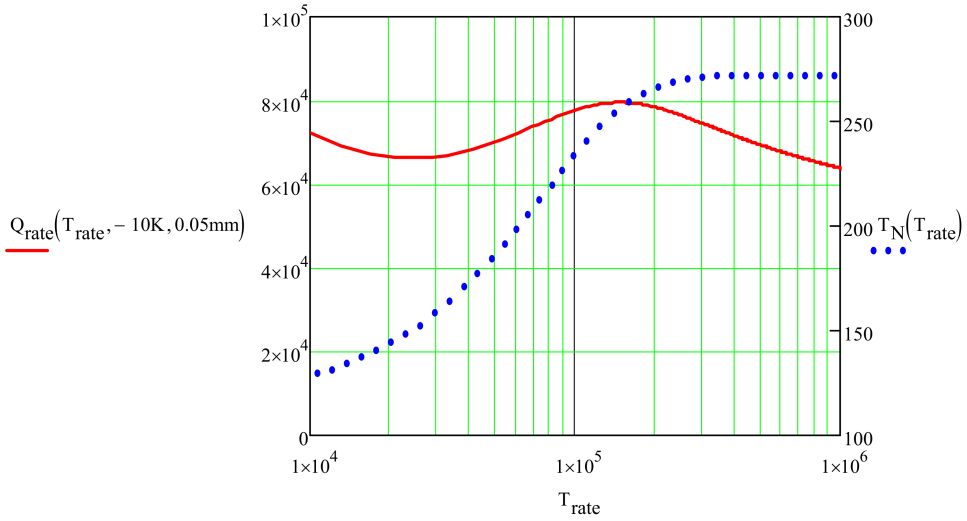


Figure 2. The minimum energy density Q_{rate} (J/m^2) calculated using Equations (2)–(6), and the water vaporization temperature T_N (°C) versus heating rate T_{rate} (K/s). The initial ice temperature was −10 °C and the ICD foil was made of 0.05 mm SS17-7PH steel.

The calculations indicate a shallow minimum in the required energy density at heating rates of approximately 2×10^4–3×10^4 K/s, corresponding to nucleation temperatures near 150 °C. This region was therefore selected as the primary design target for LTICD.

2.2. COMSOL 5.4 Modeling Validation

The analytical model presented above, based on the First Law of Thermodynamics, provides approximate design parameters for an ICD system. More accurate calculations were performed using COMSOL Multiphysics 5.4. Time-dependent simulations were carried out using the Heat Transfer in Solids and Fluids module coupled with Joule Heating, Phase Change, Solid Mechanics (including thermal stress), Electrical Circuits, Electric Currents, and Magnetic Fields. Three phases of water (ice, liquid water, and steam) and two-phase transitions (melting and vaporization) were included in the model.

Figure 3 presents a representative simulation for a 0.05 mm Ti Grade 5 foil bonded to a 0.2 mm Duralco 4703 high-temperature epoxy adhesive and covered by a 0.2 mm ice layer. The nucleation temperature was set to 150 °C, which closely corresponds to the experimentally observed threshold for this LTICD.

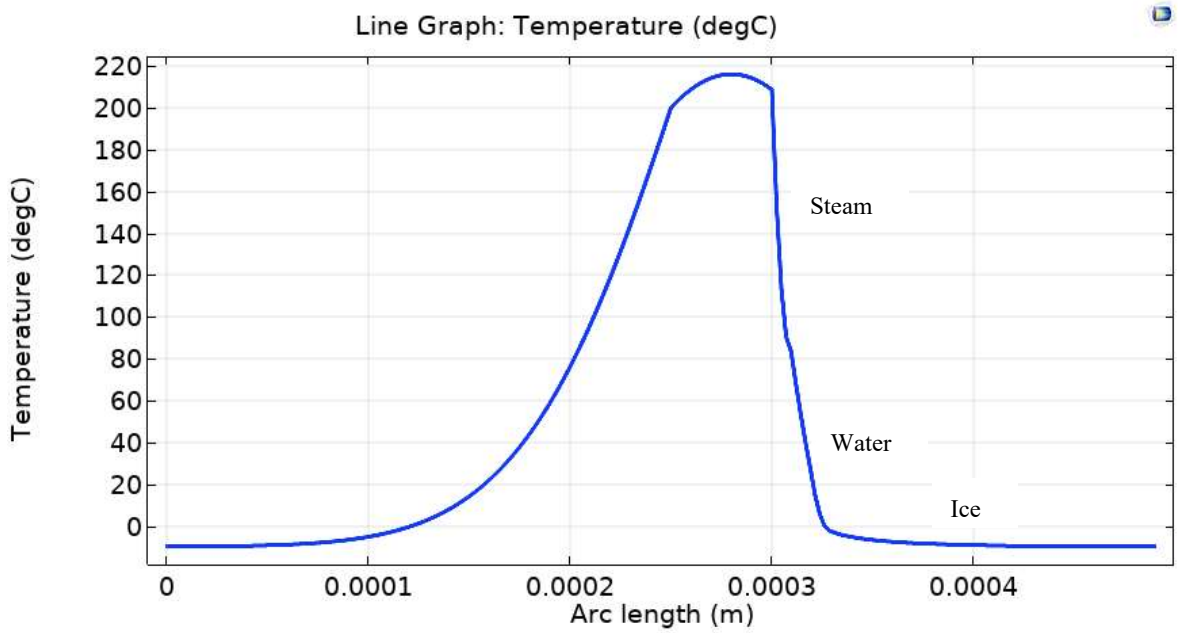


Figure 3. COMSOL Multiphysics 5.4 simulation of a 0.05 mm Ti Grade 5 ICD foil bonded to a 0.2 mm Duralco 4703 HT epoxy adhesive and covered by a 0.2 mm ice layer. Capacitance C = 35 mF, charging voltage V_0 = 300 V, energy density Qrate = 77.8 kJ/m^2, simulation time t = 2 ms, and prescribed nucleation temperature T_n = 150 °C.

The simulations revealed several important features of the ICD process. Owing to the relatively low thermal conductivity of Ti Grade 5, a significant temperature gradient developed across the foil thickness. After 2 ms of heating, approximately 5 μm of the interfacial water had vaporized, while approximately 20 μm of ice had melted. The predicted thickness of the melted layer agreed closely with the thermal diffusion length calculated using Equation (3), whereas the classical Stefan solution (Equations (5) and (6)) consistently predicted a substantially thicker melted layer. Consequently, the thermal diffusion-length approximation was adopted in the subsequent energy calculations.

2.3. Calculations of the Maximum Expansion Work by Water Vapor

The maximum mechanical work available for ice ejection was estimated by assuming an ideal isentropic expansion of the superheated water layer produced during the ICD

process. Under these conditions, the maximum expansion work equals the difference between the initial internal energy of the liquid water immediately before nucleation and the final internal energy of the resulting water/steam mixture after expansion to atmospheric pressure:

$$W_{max} = U_w(T_w) - U_w(100\ ^\circ\mathrm{C}) - U_g(100\ ^\circ\mathrm{C}) \tag{7}$$

where $U_w(T_w)$ is the internal energy of liquid water immediately before the nucleation event, $U_w(100\ ^\circ\mathrm{C})$ is the internal energy of saturated liquid water at atmospheric pressure, and $U_g(100\ ^\circ\mathrm{C})$ is the internal energy of saturated water vapor at the same pressure. The thermodynamic properties of water used in the calculations were taken from the steam tables in Ref. [15].

As a first approximation, the temperature across the thin melted water layer was assumed to vary linearly from the foil temperature, T_{ICD}, to the melting temperature at the moving water–ice interface. During the rapid pressure release, a fraction of the superheated liquid fr flashes into steam. Assuming the expansion is isentropic, the flash fraction is determined from conservation of entropy:

$$s_w(T_w) = s_w(100\ ^\circ\mathrm{C})\cdot(1 - fr) + fr\cdot s_g(100\ ^\circ\mathrm{C}) \tag{8}$$

where s_w and s_g are the specific entropies of liquid water and saturated steam, respectively. Solving Equation (8) gives:

$$fr(T_w) = \frac{s_w(T_w) - s_w(100\ ^\circ\mathrm{C})}{s_g(100\ ^\circ\mathrm{C}) - s_w(100\ ^\circ\mathrm{C})} \tag{9}$$

Figure 4 shows the calculated flash fraction as a function of the initial water temperature. As expected, the fraction of water converted into steam increases rapidly with increasing temperature. The final internal energy of the water/steam mixture is therefore:

$$U_{final}(T_w) = (1 - fr(T_w))\cdot U_w(100\ ^\circ\mathrm{C}) + fr(T_w)\cdot U_g(100\ ^\circ\mathrm{C}) \tag{10}$$

and the corresponding maximum mechanical work available from the expansion becomes:

$$W_{max}\ (Tw) = U_w\ (Tw) - U_{final}(T_w) \tag{11}$$

The expansion work per unit interface area was obtained by integrating the available work through the melted water layer:

$$\frac{W_{\max}}{A} = \rho_w \int_0^{l_w} [U_w(T(x)) - U_{\mathrm{final}}(T(x))]\cdot\rho_w dx \tag{12}$$

where A is the ice–metal contact area and l_w is the melted-layer thickness calculated from Equation (3). Assuming that all this work is converted into the kinetic energy of an ice plate of thickness t_i, the theoretical upper limit of the ice-ejection velocity is:

$$v_i = \sqrt{\frac{W_{max}}{A}\cdot\frac{2}{t_i\cdot\rho_i}} \tag{13}$$

Equation (13) represents an ideal upper limit because it assumes that all the expansion work is converted into translational kinetic energy of the ice. In practice, part of the available work is dissipated by viscous losses, shock-wave generation, deformation, and residual fluid motion.

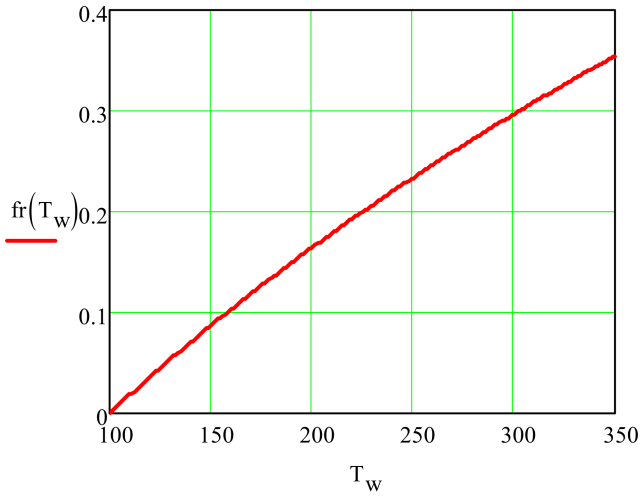


Figure 4. Water flash fraction, fr, as a function of initial water temperature, °C.

Figure 5 presents the predicted maximum velocity of a 10 mm thick ice plate together with the corresponding nucleation temperature as functions of heating rate. The calculations indicate that the theoretical maximum ice velocity reaches a broad maximum near a heating rate of approximately 2×10^5 K/s, which lies within the transition region between the low- and high-heating-rate nucleation branches. Ice-ejection velocity is governed by two competing effects as the heating rate increases. First, increasing the heating rate shortens the time available for thermal diffusion and melting before nucleation occurs; consequently, the thickness and mass of the superheated interfacial water layer decrease. This tends to reduce the mechanical work available for ice ejection. Second, the nucleation temperature increases through the transition heating-rate regime. The higher temperature increases the specific expansion work available from the superheated water and therefore tends to increase the ejection velocity. Because both dependencies are nonlinear, their competition produces the broad maximum in predicted ice velocity shown in Figure 5. At still higher heating rates, once the nucleation temperature approaches its high-temperature plateau, the decreasing thickness of the melted water layer again becomes dominant, and the predicted velocity decreases.

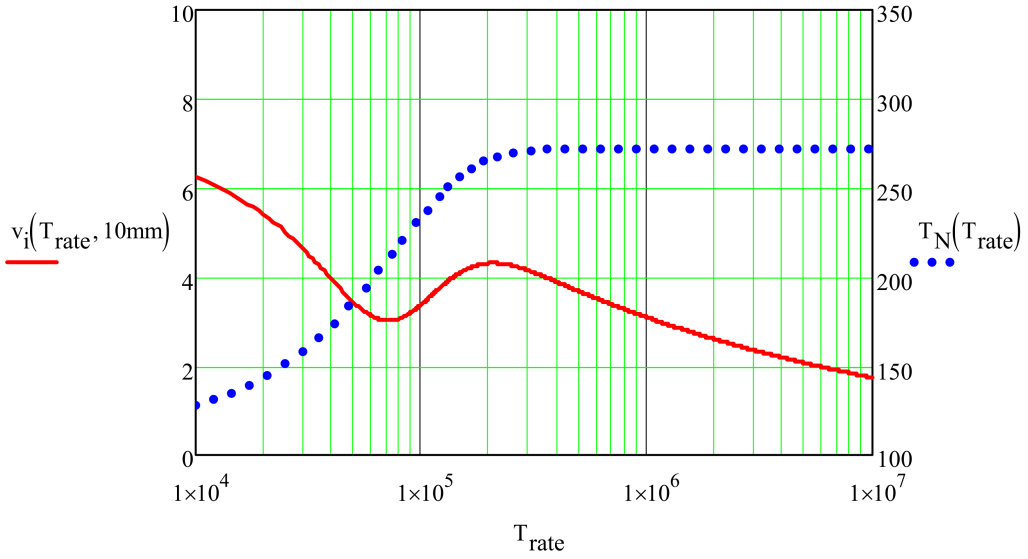


Figure 5. Dependence of the maximum velocity of 10 mm ice plate, v_i, m/s, and nucleation temperature, T_N, °C, versus ICD heating rate, °C/s. The water thickness layer l_w was calculated using Equation (3).

2.4. Overheating Ice-Free Areas of ICD

One of the principal design constraints of an ICD system is the maximum temperature reached in the ice-free regions of the foil. In these areas, the electrical energy is not consumed by melting ice or vaporizing water and therefore produces substantially higher foil temperatures than beneath the ice. If the ICD is not properly designed, the temperature in these regions may exceed the allowable service temperature of either the foil or the supporting substrate. Applying the First Law of Thermodynamics to an ice-free region gives the maximum foil temperature:

$$T_{no_ice} = \frac{Q_{ICD}}{\rho_m \cdot C_m \cdot t_m + \rho_S \cdot C_S \cdot \lambda_S} + T_0 \tag{14}$$

where T_{no_ice} is the maximum temperature of the foil in the absence of ice.

Equation (14), together with Equations (2) and (3), was used to optimize the ICD geometry and operating conditions for each foil material investigated in this study. The optimization simultaneously minimized the required ICD energy density and the maximum temperature of the ice-free regions.

Figure 6 presents a representative design optimization for a 0.05 mm Ti Grade 5 foil bonded to a Duralco 4703 high-temperature epoxy adhesive. The foil aspect ratio determines its electrical resistance and, consequently, influences the ICD heating rate and energy requirements. Therefore, the required energy density, total energy consumption, and maximum temperature reached in the ice-free regions all depend on the foil geometry.

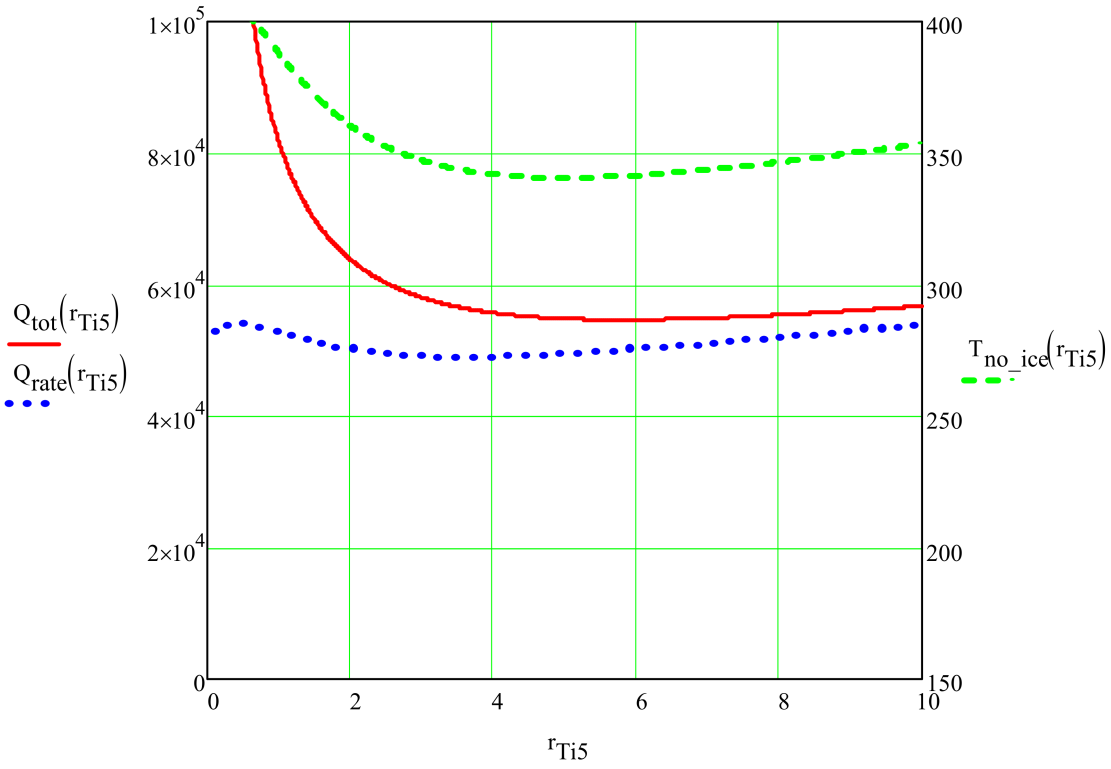


Figure 6. An example of design optimization analysis. Total energy density requirement, Q_{tot} (J/mm^2), ICD energy density requirement, Q_{rate} (J/m^2), and maximum temperature of no-ice area LTICD, as functions of ICD aspect ratio, r_{Ti5} = L/w. T_N = 150 °C. T_i = −10 °C, T_{rate} = 150C/($R_{tot}(r_{Ti5})\cdot C_C$). Titanium Grade 5 0.05 mm foil on Duralco 4703 HT epoxy adhesive. Q_{tot} includes power circuit losses. The total circuit resistance R_{tot}(rTi5) is a function of the ICD aspect ratio.

https://doi.org/10.3390/aerospace13090839

The calculations demonstrate that the optimum aspect ratio depends on the primary design objective. Designs intended to minimize energy consumption differ from those intended to minimize the maximum temperature of the ice-free regions. Consequently, the final ICD geometry represents a compromise between electrical efficiency and thermal reliability.

2.5. Thermal Stress in the Foil and Adhesive Layer

The adhesive layer plays a critical role in ICD performance. Besides attaching the foil to the supporting structure, it influences the required energy density, the maximum temperature of the ice-free regions, the thermal stress developed in the foil, and the efficiency with which the pressure impulse is transmitted to the ice layer. Consequently, thermal stresses in both the foil and the adhesive must remain below their allowable limits to ensure reliable long-term operation.

The thermal stresses generated during rapid ICD heating were estimated using the classical Volkersen shear-lag model for bonded laminates [16,17]. Assuming a thin metal foil bonded to a rigid substrate through an adhesive layer, the maximum compressive stress in the foil occurs at its center and is given by

$$\sigma_{max} = E_m \cdot \alpha_m \cdot \Delta T \cdot \left[1 - sech\left(\frac{\beta \cdot L}{2}\right)\right] \tag{15}$$

$$\beta = \sqrt{\frac{2 \cdot \mu_a}{E_m \cdot t_m \cdot t_a}} \tag{16}$$

where β is the shear-lag parameter. Here, t_m and t_a are the thicknesses of the metal foil and adhesive layer, respectively, E_m is the Young's modulus of the foil, μ_a is the adhesive shear modulus, α_m is the coefficient of thermal expansion of the foil material, and ΔT is the temperature difference between the foil and the adhesive.

The corresponding maximum shear stress in the adhesive occurs near the foil ends and is given by:

$$\tau_{max} = E_m \cdot \alpha_m \cdot \Delta T \cdot \beta \cdot t_m \cdot \left[tanh\left(\frac{\beta \cdot L}{2}\right)\right] \tag{17}$$

The calculations assumed that the ICD heating pulse is sufficiently short that only a thin thermal diffusion layer of the adhesive is heated, while the remaining adhesive thickness remains close to its initial temperature. This approximation is consistent with the short heating times and the thermal diffusion lengths predicted by the COMSOL simulations.

Figures 7 and 8 present calculated thermal stresses for laminates consisting of 0.076 mm SS17-7PH foil bonded to a 1 mm layer of four representative high-temperature adhesives.

Figure 7 shows the maximum compressive stress developed in the foil. The calculated stresses remain below the elevated-temperature yield strength of SS17-7PH for the more compliant adhesive systems, whereas stiffer ceramic adhesives produce substantially higher thermal stresses.

Figure 8 shows the corresponding maximum shear stress in the adhesive layer. Softer adhesives experience relatively low interfacial shear stresses, whereas high-modulus ceramic adhesives develop considerably larger stresses that may approach their bond-strength limits for long foils. These results demonstrate that adhesive mechanical properties are as important as their thermal resistance when designing reliable ICD systems.

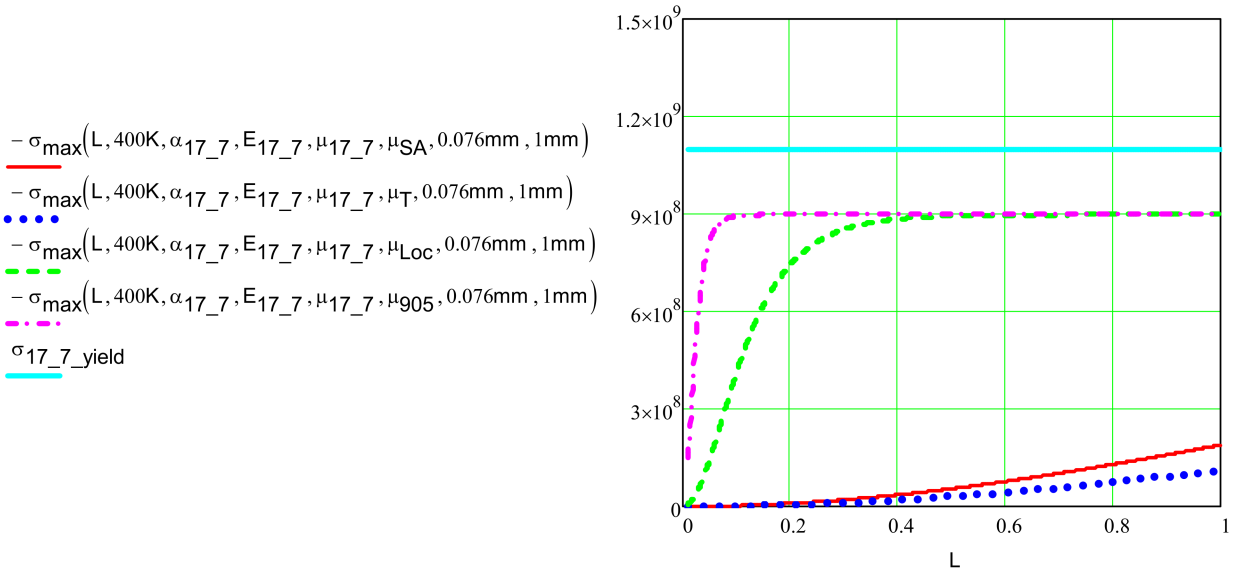


Figure 7. Maximum tangential compressive stress σ_{max}, Pa, in 0.076 mm SS17-7PH steel foil versus foil length, L, m. Silicone Permatex Optimum 399 ($_{SA}$, solid red line), 3M HT VHB 4646 tape ($_{T}$, blue dotted line), Loctite 2000 composite adhesive ($_{Loc}$, green dashed line), and Resbond 905 ceramic adhesive ($_{905}$, magenta dash-dotted line). SS17-7PHCH900 yield stress at 400 °C (17_7_yield, solid green line) is shown as a reference. The thickness of all adhesive layers was 1 mm. The maximum stress in the laminates was calculated using Equation (16).

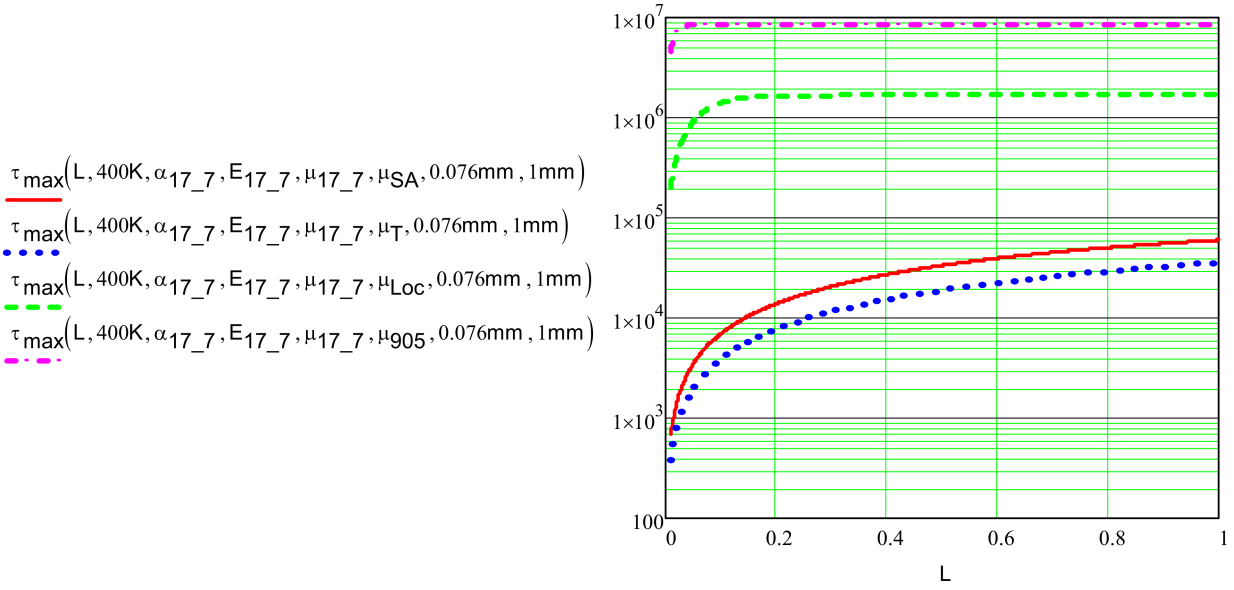


Figure 8. Maximum shear stress τmax, Pa, in a 1 mm adhesive layer versus foil length, L, m. Silicone Permatex Optimum 399 ($_{SA}$, solid red line), 3M HT VHB 4646 tape ($_{T}$, blue dotted line), Loctite 2000 composite adhesive ($_{Loc}$, green dashed line), and Resbond 905 ceramic adhesive ($_{905}$, magenta dash-dotted line). The maximum shear stress in the laminates was calculated using Equation (17).

Although the adhesive layer is 1 mm thick, the short duration of the ICD pulse limits heat penetration to only several tens of micrometers. Consequently, most of the adhesive remains near the initial temperature and acts as a mechanically rigid support during the pulse.

3. Experimental Work

All experiments were conducted at the Ice Research Lab of Petrenko-Multiphysics LLC. Various metals and metal alloys were evaluated theoretically to identify suitable foil and substrate materials for experimental testing. A detailed description of the experimental setup, materials, and electronics is provided in Sections 3.1–3.4. A general view of the ICD inside the refrigerator is shown in the Supplementary Video Clip. The information provided is intended to facilitate reproduction of the experiments.

3.1. Metals Selection and Preparation

Cold-rolled Titanium Grade 5 (Al 6%, V 4%) is a titanium alloy known for its very high mechanical strength and high electrical resistivity. It also has a very low $C_m \cdot \rho_m$ product, a CTE approximately one-half that of SS304 and SS316 stainless steels, and high corrosion resistance up to 426 °C. After UV treatment, it demonstrated a near-zero water contact angle. The titanium surface was degreased with acetone and isopropyl alcohol and then exposed to 254 nm UV (no-ozone) light for 1–12 h. This treatment produced a durable hydrophilic surface. The 0.1 mm thick nickel-foil bus bars (BB) were connected to the titanium ICD foils using a double-pulse spot welder. The BB/Ti contact resistance was approximately 1 mΩ for each bus bar, each containing 20 spot-weld nuggets.

Cold-rolled 17-7PHC stainless steel was selected for its exceptional strength, high electrical resistivity, lower CTE than that of SS304/316, and high corrosion resistance. The SS17-7PH surface was degreased with acetone and isopropyl alcohol, polished with 1500-grit sandpaper, and rinsed in distilled water. The treatment produced a hydrophilic surface that had to be restored daily. A more robust hydrophilic surface on SS17-7PH can be produced using nanoscale Sol-Gel SiO_2–TiO_2 coating technology, which has been used to create self-cleaning hydrophilic stainless-steel surfaces [18]. Additional exposure to 254 nm UV radiation for 4 h did not improve the hydrophilicity of the stainless steel. The samples were usually iced within 30 min after treatment.

Titanium Grade 5 samples, although tested daily, did not require repeated cleaning and retained their hydrophilic properties. SS17-7PH foils were re-abraded between LTICD tests. HTICD testing cleaned all the samples well.

Table 1 presents properties of the metals used in this study.

Table 1. Metals used in this study. $\sigma_{TS} = \alpha_m \cdot E_m \cdot 400$ K, MPa.

Metal	$\sigma_{TS}/\sigma_{yield}$ at 400 °C	ρ_e, ohm·m Experimental	Oxidation Resistance to Intermittent 400 °C Pulses
Ti Grade 5, cold worked	0.66	1.64×10^{-6}	High
Ti Grade 3 cold worked	1.32	0.52×10^{-6}	High
Copper	1.92	1.72×10^{-8}	High
Invar	0.24	0.82×10^{-6}	modest
SS17_7PH	0.63	1.02×10^{-6}	High
SS304, cold rolled thin foil	1.34	0.72×10^{-6}	High
Tantalum cold worked	0.825	1.35×10^{-7}	High

3.2. Substrate Materials Selection

Adhesives that can withstand temperatures at and above 400 °C are primarily based on inorganic components, such as ceramics (CA), glass, or silicates (Si). These materials, while exceptionally heat-resistant (only when they are slowly heated), form rigid and brittle

bonds with metals rather than elastic ones. They are also more likely to fail under thermal shock or stress because of their significant CTE and low flexibility.

Cotronics 905, a silicate-based adhesive specifically designed to withstand thermal shock, is an exception. After evaluating many commercially available ceramic (CA) and silicone adhesives (SA), only two were selected. The first was Cotronics 905, a silicate-based, very-low-CTE, thermal-shock-resistant adhesive. The second was Permatex Optimum silicone adhesive, with a maximum intermittent temperature of Tmax = 399 °C. SA Duraseal 1531 (Tmax = 427 °C) may provide even greater temperature capability, but wide, thin layers require more than one month to cure at room temperature, making it inconvenient for laboratory testing. An array of thin (2 mm) neodymium permanent magnets covered with 50 μm single-sided Kapton film was used to test ferromagnetic stainless-steel and Invar foils. Permatex silicone adhesive demonstrated very high adhesion strength and withstood several dozen ICD pulses without signs of damage or delamination. Table 2 presents properties of the adhesives used in this study.

Table 2. Adhesives used in this study. NA is used for "Not Available".

Adhesive	ρ kg/m^3	C J/(kg·K)	k W/(m·K)	E GPa	α 10^{-5}/K	$\sqrt{\rho kC}$ Kg^2/(s^5·K^2)	σ_{bond} MPa	σ_{max} MPa	T_{max} °C
CA Resbond 905	1310	800	1.44	7.5	0.054	1228	22	22	1370
CA Resbond 907	1281	1050	0.865	190	3.9	1080	4	24	1306
Permatex Optimum	1180	1050	0.2	0.0014	30	665	2.8	1.9	399
Duraseal 1531	998	1465	0.3	0.0012	2	1710	1.9	NA	427
Duralco 4703	1800	1043	2.59	5	2.6	2200	21	NA	343
3M 4646 tape	840	1000	0.11	520 kPa	18	304	0.69	NA	232

3.3. Measurements of Ice Velocity

Two methods were used to measure the maximum initial velocity of the ice fragments. In the first method, video clips of ICD deicing were examined frame by frame at intervals of 1/60 s. During the ICD tests, the ice fragments were propelled rapidly away from the deicing surface. In many demonstrations, the fragments reached velocities on the order of 10 m/s. At typical smartphone frame rates (30–60 fps), the fragments move approximately 0.17–1 m per frame and therefore leave the field of view within 1–2 frames. This temporal resolution is insufficient for accurate frame-based tracking. Therefore, video footage was used primarily for qualitative confirmation of ICD performance.

In the second method, the initial horizontal velocity v_{ice} was obtained using a simple ballistic equation. The ICD was positioned 1.0 m above the carpeted floor, and the horizontal travel distance x of the detached ice fragments was measured. Assuming a negligible initial vertical velocity, the flight time is determined by free fall:

$$t = \sqrt{\frac{2h}{g}} \tag{18}$$

where $h = 1.0$ m and $g = 9.81$ m/s^2.

The initial horizontal velocity is then expressed as

$$v_{ice} = \frac{x}{t} = x\sqrt{\frac{g}{2h}} \tag{19}$$

This method significantly improves the precision of the velocity measurements compared with frame counting. For the demonstrated ICD configurations, the measured veloci-

ties were typically in the range shown above. These experimental results agree well with the theoretical estimates based on vapor-expansion impulse generation. $v_{ice} \approx 1$–10 m/s.

3.4. Electronics

Figure 9 shows the electrical circuit used in this study. The MOC223 optocoupler isolates the low-voltage trigger circuit (left) from the high-voltage ICD circuit (right). The two diodes protect the capacitor and thyristor-diode module MCD312-12io1 (SCR) from reverse-voltage peaks. The peak capacitor-discharge currents during testing varied from 200 A to 10 kA. Because of the low resistance of the tested ICDs, most connections were soldered, and 12 and 14 AWG leads were used to minimize the total resistance in the high-current circuits. The capacitor charger module delivered an output power of 60 W with a maximum output voltage of 900 V. The film capacitors used in this study (0.1–3 mF) had a very low estimated equivalent series resistance (ESR) of approximately 1 mΩ. The large aluminum electrolytic capacitors (15 and 35 mF) had an ESR of approximately 5 mΩ. The circuit shown in Figure 9 was used for several hundred pulses during the testing period. A two-channel digital oscilloscope recorded the ICD voltage and current, and a digital voltmeter was used to monitor the initial capacitor voltage.

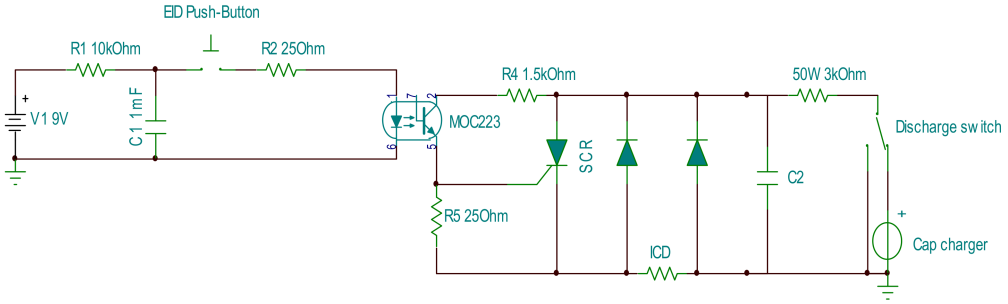


Figure 9. Schematic diagram of the electronics used to test the ICD prototypes.

3.5. Experimental Results

T_{rate} was calculated as $T_{ICD}/(R_{tot} \cdot C)$, where R_{tot} is the total power-circuit resistance.

T_{ICD} and T_{no_ice} were calculated using the experimental Q_{ICD} values and the energy-conservation law (Equation (2)).

At the thresholds (shown in bold in Table 3), $T_{ICD} = T_N$. The threshold temperature was $T_{ICD} = 144.5$ °C at $Q_{ICD} = 40$ kJ/m^2 for the 0.05 mm Ti Grade 5 foil powered by a 35 mF capacitor, and $T_{ICD} = 160$ °C at $Q_{ICD} = 80$ kJ/m^2 for the 0.105 mm Ti Grade 5 foil powered by a 15 mF capacitor.

Table 3 summarizes representative experiments covering the complete range of ICD operating conditions investigated in this study. The selected results include LTICD, MTICD, and HTICD configurations employing different foil materials, geometries, and capacitor banks. For each experiment, the measured ice-ejection velocity is compared with the corresponding energy density, COMSOL-predicted temperatures, and estimated heating rate.

Figure 10 shows the dependence of the maximum ice-cube ejection velocity on the ICD energy density, Q_{rate}, for ICDs made from two Ti Grade 5 foils of different thicknesses. As shown in Table 3, the gradual increase in Qrate shifted the ICD operating mode from LTICD toward HTICD.

Table 3. Selected experimental results.

Size, mm	V_0	C	Q_{rate}	T_{ICD} °C	T_{no_ice}	v_i	T_{rate}
	V	mF	kJ/m^2	°C, COMSOL	°C, COMSOL	m/s	K/s
SS17-7PHC							
0.05 × 40 × 210 SS17-7PH, on Kapton	170	35	51	130	245	0.4	3.2×10^4
0.05 × 40 × 210 SS17-7PH, on Kapton	180	35	57.5	148	276	0.6	3.6×10^4
0.05 × 40 × 210 SS17-7PH, on Kapton	200	35	71	184	342	1.4	4.44×10^4
0.05 × 40 × 210 SS17-7PH, on Kapton	220	35	86	223	414	2	5.55×10^4
0.05 × 40 × 210 SS17-7PH on Kapton	250	35	96	248	462	3	5.92×10^4
0.05 × 40 × 210 SS17-7PH on Kapton	290	15	58	182	284	1.4	1.02×10^5
0.05 × 40 × 210 SS17-7PH on Kapton	350	15	84	264	416	3	1.46×10^5
0.076 × 20 × 150 SS17-7PH on 907	700	1.5	115	358	404	6	2.2×10^6
0.076 × 20 × 150 SS17-7PH on 907	720	1.5	136	423	479	8	2.6×10^6
0.076 × 20 × 150 SS17-7PH on 907	760	1.5	139	432	490	10	2.6×10^6
0.076 × 20 × 150 SS17-7PH on 907	760	1.5	139	432	490	6	2.6×10^6
0.076 × 20 × 150 SS17-7PH on 907	700	1.5	117	364	411	3.9	2.2×10^6
0.076 × 20 × 150 SS17-7PH on 907	675	1.5	110	342	386	2	2.1×10^6
0.0257 × 25.4 × 38 SS304 on 3M 4611	314	0.383	19.6	≈300	-	1	9.0×10^6
Titanium Grade 5 and 1, substrate				3M/905/4703	3M/905/4703		
0.05 × 50 × 85 Ti5 on 3M 4646, UV	190	35	102	413/332/281	689/477/360	6.6	1.12×10^5
0.05 × 50 × 85 Ti5 on 3M 4646, UV	175	35	86.6	330/280/223	584/404/304	4.4	9.64×10^4
0.05 × 50 × 85 Ti5 on 3M 4646, UV	160	35	72.4	278/220/173	486/336/253	2.2	8.14×10^4
0.05 × 50 × 85 Ti5 on 3M 4646, UV	150	35	63.6	213/175/143	426/294/222	1.6	7.14×10^4
0.05 × 50 × 85 Ti5 on 3M 4646, UV	135	35	51.5	153/124/104	343/237/177	0	5.82×10^4
0.105 × 25 × 185 Ti5 on 3M 4611, UV	250	15	83.7	165	301	0.35	8.3×10^4

Table 3. *Cont.*

Size, mm	V_0	C	Q_{rate}	T_{ICD} °C	T_{no_ice}	v_i	T_{rate}
	V	mF	kJ/m^2	°C, COMSOL	°C, COMSOL	m/s	K/s
0.105 × 25 × 185 Ti5 on 3M 4611, UV	275	15	101	247	366	1	9.95×10^4
0.105 × 25 × 185 Ti5 on 3M 4611, UV	300	15	120	293	436	2.4	1.17×10^5
0.01 × 37 × 75 Ti1 on Porcelain	790	0.1	11.3	≈300	-	2	2.5×10^7
0.05 × 25 140 Invar on 3M 4646	160	35	101	177	304	2	4.3×10^4

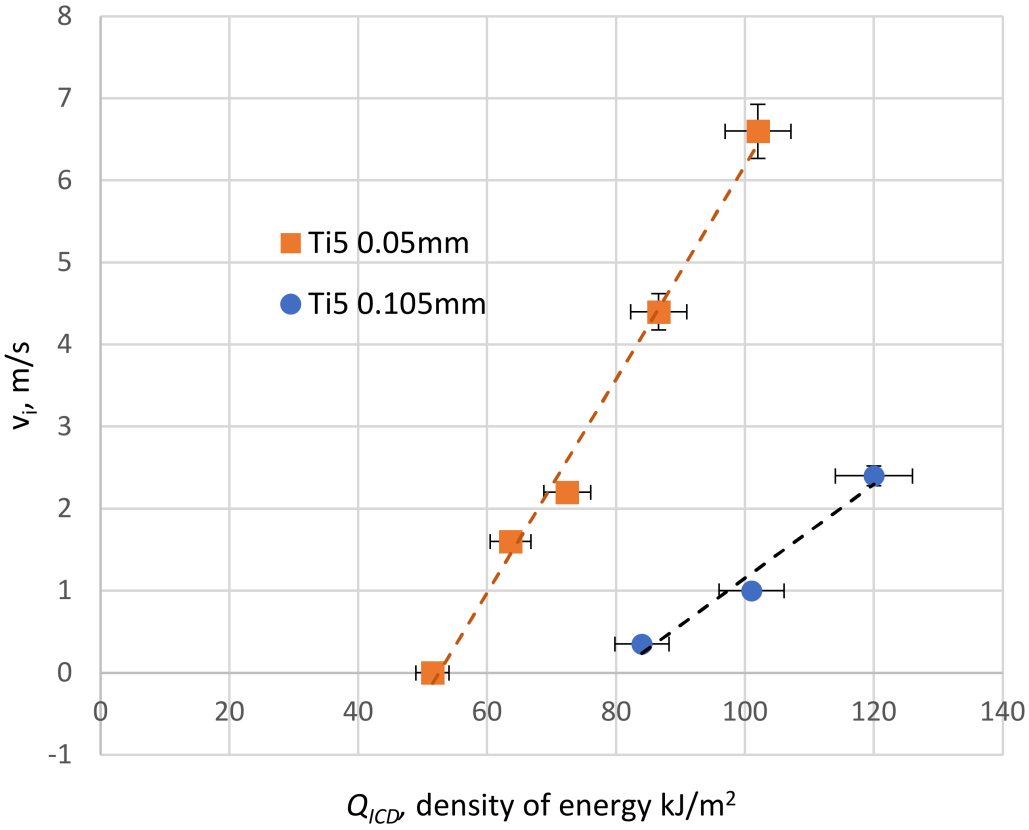


Figure 10. Maximum ice-cube ejection velocity, m/s, versus ICD energy density Q_{ICD}, kJ/m^2, for Ti Grade 5.

Figure 11 shows the dependence of the maximum ice-cube ejection velocity on the ICD energy density, Q_{rate}, for ICDs made from two SS17-7PH foils of different thicknesses and powered by different capacitors. As shown in Table 3, the gradual increase in Qrate shifted the ICD operating mode from LTICD toward HTICD.

Figure 12 shows the dependence of the maximum ice-cube ejection velocity on the heating rate.

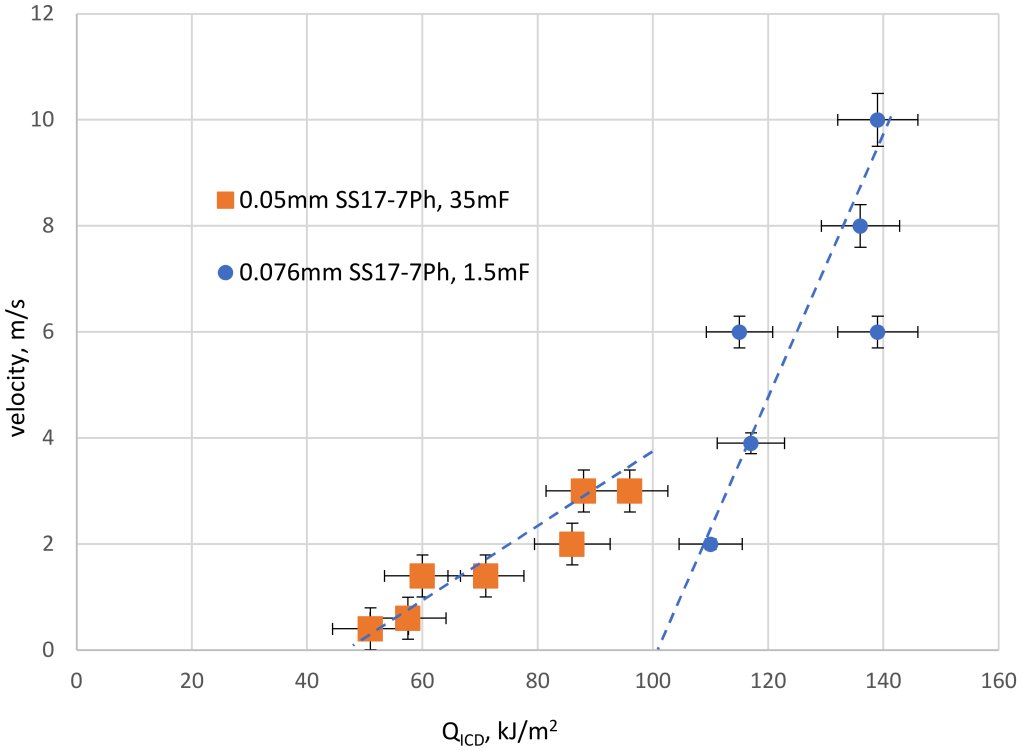


Figure 11. Maximum ice-cube ejection velocity, m/s, versus ICD energy density Q_{ICD}, kJ/m^2, for SS17-7PH.

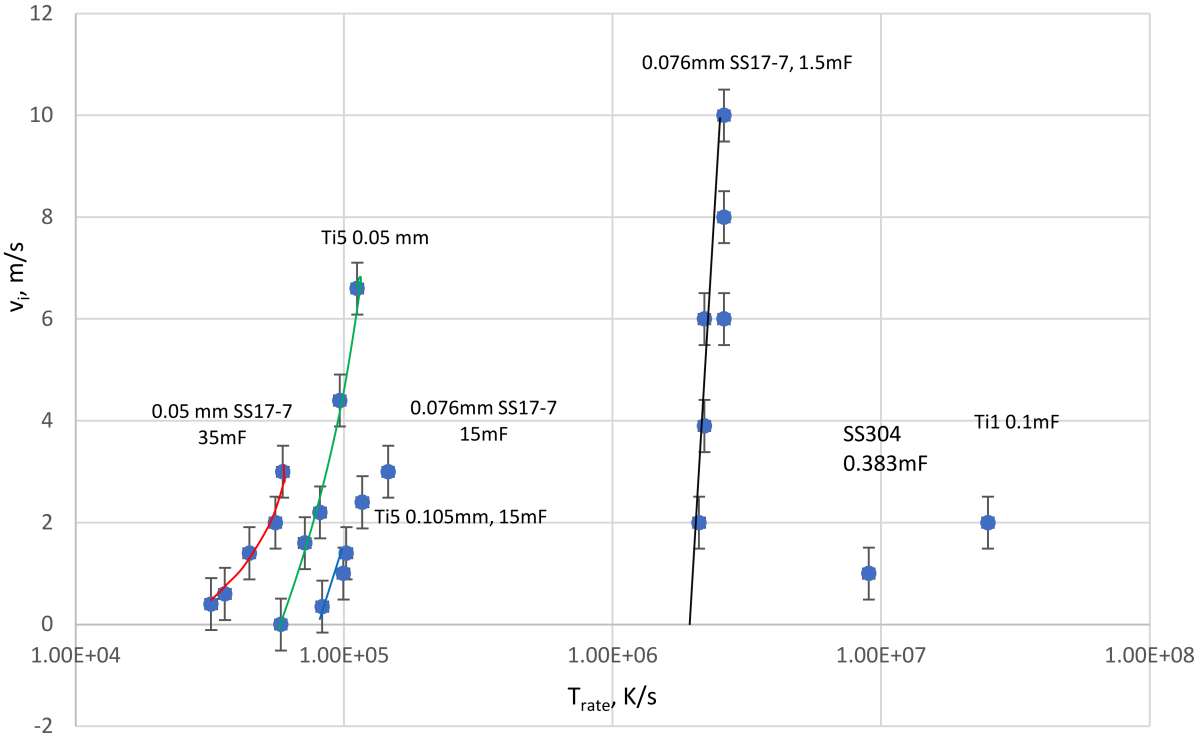


Figure 12. Maximum ejection velocity, m/s, of 1 cm^3 ice cubes versus heating rate, K/s. Trate was calculated as $T_{ICD}/(R_{tot} \cdot C)$, where R_{tot} is the total power-circuit resistance.

3.6. Principal Experimental Findings

The experimental investigation led to the following principal observations.

- Explosive vaporization of the melted interfacial water layer was reproducibly observed whenever the applied ICD energy density exceeded the threshold value for a given foil material, geometry, and heating rate.
- For every material and capacitor combination, the ice-cube ejection velocity increased monotonically with increasing ICD energy density (Figures 10 and 11).
- The majority of successful LTICD and MTICD experiments were conducted within the intermediate heating-rate range of approximately 10^4–10^6 K/s identified by Skripov et al. [10].
- The experimentally determined threshold temperatures approximately followed the heating-rate dependence of the nucleation temperature shown in Figure 1.
- Hydrophilic foil surfaces consistently produced higher and more reproducible ice-ejection velocities than untreated hydrophobic surfaces.
- Functional Low-Temperature, Medium-Temperature, and High-Temperature Ice Cavitation Deicing (LTICD, MTICD, and HTICD) systems were successfully designed and experimentally demonstrated.
- Equation (13) provided reasonable estimates of the experimentally observed ice-ejection velocities for LTICD and MTICD (approximately 2–4 m/s). The model was less accurate for HTICD, where cavitation pressures substantially exceed the equilibrium vapor pressure assumed in the present analysis [8,9].
- Once the threshold energy density had been exceeded, ice cubes were consistently ejected with velocities ranging from approximately 1 to 10 m/s, depending on the applied ICD energy density.

3.7. Engineering Observations

The experiments also provided several practical design recommendations.

- Permatex Optimum 399 silicone adhesive demonstrated the best combination of reliability and durability, although complete curing required several days.
- 3M HT VHB tape performed well up to maximum intermittent temperatures of approximately 300 °C, exceeding its nominal continuous service temperature.
- Magnetic support proved to be highly effective for ferromagnetic foils (SS17-7PH, SS430, and Invar). Although slight foil displacement occurred during the ICD pulse, full contact was restored within approximately one second.
- Thermal strains were greatest near the massive electrical bus bars. This effect can be reduced by using thinner bus bars that are heated by the same discharge current, thereby reducing differential thermal expansion.
- Compared with HTICD, LTICD required approximately one-half of the operating voltage and one-fifth of the peak current.
- The use of high-capacitance aluminum electrolytic capacitors increased the area deiced by a single pulse by approximately one order of magnitude compared with the original HTICD implementation.

4. Discussion

The present investigation demonstrates that ice cavitation deicing is not limited to the high-temperature regime previously reported for HTICD [7]. By operating in the intermediate heating-rate region identified by Skripov et al. [10], efficient cavitation deicing was achieved at substantially lower temperatures while preserving the fundamental mechanism of rapid vapor generation and impulse loading of the ice layer.

The experimental and analytical results indicate that LTICD operating near $T_N \approx 150$ °C provides the best overall engineering compromise. At this operating point, the required energy density is near its minimum, the maximum temperature of the ice-free re-

gions remains moderate, thermal stresses are substantially reduced, and useful ice-ejection velocities of up to approximately 3 m/s were obtained. These prototypes demonstrated stable and reproducible operation and therefore represent the preferred LTICD design.

Operation in the transition and high-heating-rate regimes produced considerably higher ice-ejection velocities, reaching 10 m/s for HTICD. These improvements, however, were accompanied by significantly higher foil temperatures, larger pulse currents, and increased thermal stress. Consequently, the transition regime appears to offer opportunities for further optimization, whereas the present results suggest that operation near $T_N \approx 150\ ^\circ\mathrm{C}$ and $\dot{T} \approx 4 \times 10^4$ K/s provides the most practical balance between performance and reliability.

Among the materials investigated, Ti Grade 5 and SS17-7PH provided the most favorable combination of electrical, thermal, and mechanical properties. In addition, the development of a reliable two-pulse spot-welding procedure for joining nickel bus bars to titanium foils solved a long-standing practical problem associated with titanium-based ICD systems. Ultraviolet treatment of titanium also significantly improved deicing performance, most likely through improved surface wettability.

The experiments further suggest that the heater surface should be regarded as an active nucleation surface rather than a passive thermal boundary. Controlled micro-roughening or shallow micro-grooving may provide stable heterogeneous nucleation sites, thereby reducing sensitivity to surface contamination, polishing condition, and oxide morphology. Such surface engineering may improve the repeatability of LTICD operation while maintaining explosive boiling near 150 °C.

Although LTICD is expected to exhibit a degree of self-cleaning through thermal desorption, vapor generation, and subcritical-water cleaning, this effect is likely to be less pronounced than in HTICD operating at 300–350 °C. LTICD should therefore remove loosely adhered contaminants effectively but should not be expected to eliminate strongly adsorbed hydrocarbon or hydraulic-fluid films as efficiently as HTICD.

Compared with HTICD, LTICD offers several important engineering advantages. The lower operating temperature substantially expands the range of suitable adhesive systems and structural materials while reducing thermal stresses in both the foil and adhesive layer. Lower operating voltages and pulse currents simplify the power electronics, and the use of large aluminum electrolytic capacitors makes it possible to store significantly more energy than practical HTICD systems. This enables considerably larger deicing areas to be protected by a single discharge pulse.

HTICD nevertheless retains important advantages. Its higher operating temperature produces stronger pressure pulses and higher initial steam pressures, which are beneficial for fragmenting thick or strongly adhered ice. The higher temperatures also provide a more aggressive self-cleaning action of the heater surface.

Overall, the present work extends the concept of ice cavitation deicing from a proof-of-concept high-temperature technology to a broader family of deicing systems operating over a wide range of heating rates and temperatures. While HTICD established the feasibility of cavitation deicing, the present results demonstrate that the same physical mechanism can be implemented using substantially lower temperatures and a more practical electrical architecture, making LTICD and MTICD promising candidates for future aircraft ice-protection systems.

5. Conclusions

This study developed and experimentally validated Low-Temperature Ice Cavitation Deicing (LTICD) and Medium-Temperature Ice Cavitation Deicing (MTICD) as new variants of Ice Cavitation Deicing (ICD). An analytical design methodology based on energy

conservation, transient heat transfer, thermal-stress analysis, and finite-element modeling was developed and successfully applied to the design of LTICD, MTICD, and HTICD prototypes. For the LTICD and MTICD regimes, Equation (13) predicts ice-ejection velocities of approximately 2–4 m/s, comparable with the approximately 1–4 m/s range observed experimentally under representative low- and intermediate-temperature operating conditions (Table 3). This order-of-magnitude agreement supports the use of the analytical model as a practical engineering design tool. The model is less accurate for HTICD, where cavitation pressures can substantially exceed the equilibrium vapor pressure assumed in the analysis. The experimental results demonstrate that efficient impulse cavitation deicing can be achieved at substantially lower operating temperatures than previously required for HTICD. Compared with HTICD, LTICD and MTICD reduced the required energy by approximately a factor of two and lowered both the operating and maximum heater temperatures by more than 100 °C while maintaining effective ice removal. Operating in the intermediate heating-rate regime also reduced thermal stresses, lowered the required operating voltage and pulse current, and enabled the use of high-capacitance aluminum electrolytic capacitors, increasing the deiced area achievable with a single discharge pulse by approximately one order of magnitude.

Although HTICD remains advantageous where very high-pressure impulses and aggressive self-cleaning are required, the present work demonstrates that the same cavitation-deicing mechanism can be implemented using substantially lower temperatures and a more practical electrical architecture. These results extend ice cavitation deicing from a proof-of-concept high-temperature technology to a broader family of potentially practical deicing systems suitable for future aircraft ice-protection applications.

Supplementary Materials: The following supporting information can be downloaded at: https://www.mdpi.com/article/10.3390/aerospace13090839/s1, Supplementary Video S1. Representative LTICD experiment showing the removal of 10 mm ice cubes from a 0.105 mm Ti Grade 5 foil.

Funding: This research was funded by Petrenko-Multiphysics, LLC.

Data Availability Statement: Data supporting the findings of this study are available from the author upon reasonable request.

Acknowledgments: The author gratefully acknowledges the funding and laboratory facilities provided for this research by Petrenko-Multiphysics LLC.

Conflicts of Interest: The author declares no conflict of interest.

References

1. Gent, R.W.; Dart, N.P.; Cansdale, J.T. Aircraft Icing. *Phil. Trans. R. Soc. Lond. A* **2000**, *358*, 2873–2911. [CrossRef]
2. Petrenko, V.F. Systems and Methods for Modifying an Ice-to-Object Interface. U.S. Patent 6,870,139, 22 March 2005.
3. Petrenko, V.F.; Sullivan, C.R.; Kozlyuk, V.; Petrenko, F.V.; Veerasamy, V. Pulse electro-thermal de-icer (PETD). *Cold Reg. Sci. Technol.* **2011**, *65*, 70–78. [CrossRef]
4. Meier, O.; Scholz, D. *Handbook Method for Estimating Power Requirements for Electrical De-Icing Systems*; Hamburg University of Applied Sciences: Hamburg, Germany, 2010. Available online: https://www.fzt.haw-hamburg.de/pers/Scholz/MOZART/MOZART_PRE_DLRK_10-08-31.pdf (accessed on 10 September 2026).
5. *SAE: Ice, Rain, Fog, and Frost Protection*; Society of Automotive Engineers: Warrendale, PA, USA, 1990; AIR 1168/4.
6. Khodakarami, S.; Agarwal, V.; Kabirzadeh, P.; Solecki, A.; Hoque, M.J.; Yang, W.; Stokowski, N.; Jacobs, J.; Chatterji, A.; Lovelace, E.; et al. Aircraft Electrothermal Pulse Deicing. *J. Heat Mass Transf.* **2025**, *147*, 012401. [CrossRef]
7. Petrenko, V.F. Ice Cavitation Deicing for Aerospace Applications. *Aerospace* **2026**, *13*, 217. [CrossRef]
8. Caupin, F.; Herbert, E. Cavitation in water: A review. *Comptes Rendus Phys.* **2006**, *7*, 1000–1017. [CrossRef]
9. Caupin, F. Liquid-vapor interface, cavitation, and the phase diagram of water. *Phys. Rev. E* **2005**, *71*, 051605-1–051605-5. [CrossRef] [PubMed]
10. Skripov, P.V.; Bar-Kohany, T.; Antonov, D.V.; Strizhak, P.A.; Sazhin, S.S. Approximations for the nucleation temperature of water. *Int. J. Heat Mass Transf.* **2023**, *207*, 123970. [CrossRef]

11. Shoji, M.; Ueno, I.; Yamazaki, M.; Wakamatsu, K. Pressure generation by rapid heating of a metal wire in water. *Trans. Jpn. Soc. Mech. Eng. Ser. B* **1996**, *62*, 2331–2337. [CrossRef]
12. Sazhin, S.S.; Bar-Kohany, T.; Nissar, Z.; Antonov, P.A.; Strizhak, P.A.; Rybdylova, O.D. A new approach to modelling micro-explosions in composite droplets. *Int. J. Heat Mass Transf.* **2020**, *161*, 120238. [CrossRef]
13. Alexiades, V.; Solomon, A.D. *Mathematical Modeling of Melting and Freezing Processes, Chapter 2*; Hemisphere Publishing: Washington, DC, USA; CRC Press Reprint: Boca Raton, FL, USA, 1993.
14. Crank, J. *Free and Moving Boundary Problems*; Clarendon Press: Oxford, UK, 1984.
15. Wagner, W.; Kretzschmar, H.-J. *International Steam Tables: Properties of Water and Steam Based on the Industrial Formulation IAPWS-IF97*; Springer International Publishing: Berlin/Heidelberg, Germany, 2008.
16. Volkersen, O. Die Nietkraftverteilung in zugbeanspruchten Nietverbindungen mit konstanten Laschenquerschnitten. *Luftfahrtforschung* **1938**, *15*, 41–47.
17. da Silva, L.F.M.; Oechsner, A.; Adams, R.D. *Handbook of Adhesion Technology*; Springer: Cham, Switzerland, 2018.
18. Boroujeny, B.S.; Afshar, A.; Dolati, A. Photoactive and self-cleaning TiO_2–SiO_2 thin films on 316L stainless steel. *Thin Solid Films* **2012**, *520*, 6355–6360. [CrossRef]

Disclaimer/Publisher's Note: The statements, opinions and data contained in all publications are solely those of the individual author(s) and contributor(s) and not of MDPI and/or the editor(s). MDPI and/or the editor(s) disclaim responsibility for any injury to people or property resulting from any ideas, methods, instructions or products referred to in the content.